JOURNAL OF PROPULSION AND POWER
Vol. 26, No. 1, January–February 2010

Numerical Rebuilding of SMART-1 Hall Effect Thruster Plasma Plume

A. Passaro,[*] A. Vicini,[†] F. Nania,[‡] and L. Biagioni[§]
Alta SpA, 56121 Pisa, Italy

DOI: 10.2514/1.36821

The SMART-1 flight data provided an excellent opportunity for extending validation of plume prediction codes to actual flight conditions. This paper will present the results obtained for the numerical simulation of the SMART-1 plasma plume using the PICPluS particle in cell code, which had been previously validated using ground experiment data. This activity can be considered as the first important step in the direction of a full in-flight validation for the code models and algorithms. A description of the implemented physical models is provided, followed by simulation results of experimental data from Alta's tests and from the literature. Finally, the results of the code application to the SMART-1 mission are presented, focusing on the simulation of retarding potential analyzer measurement, spacecraft floating potential, and interaction of the plasma field with the satellite (in particular the solar array). The results show that, although the possibility of dangerous interaction between the electric propulsion system and the spacecraft is very limited, a number of complex phenomena arise due to the use of the electric propulsion system in orbit. For example, the interaction between the plume and the solar array orientation leads to complex patterns for the spacecraft floating potential. Eventually, full three-dimensional simulation is therefore needed to accurately model this kind of phenomena with a realistic description of the involved geometries.

Nomenclature

e = electron charge, C
k = Boltzman constant, J/K
I = current, A
n = number density, m^{-3}
P = probability, -
r = position vector, m
T = temperature, K
Vd = discharge potential, V
ε, $\varepsilon 0$ = dielectric constant, F/m
ρ = charge density, $\mathrm{C/m}^3$
Φ, φ = electric scalar potential, V

I. Introduction

ELECTRIC propulsion represents one of the most promising technologies for application to present and future space missions. In recent years, a significant number of U.S. and western European missions have seen successful use of Gridded Ion Engines (Deep Space 1, ARTEMIS, and Dawn, as well as commercial geostationary Earth orbit [GEO] spacecraft) and Hall effect thrusters (SMART-1, TacSat-2, and commercial GEO spacecraft). In the upcoming years, other major space undertakings will take advantage of electric propulsion performance, such as the European Space Agency's cornerstone mission to Mercury (Bepi Colombo), which will require significant advances in the understanding and prediction capability of interactions between the spacecraft and the engine plume.

As the European Space Agency SMART-1 mission proved, although the possible dangerous interaction between the electric propulsion system and the spacecraft is very limited, many complex phenomena arise due to the extensive use of the propulsion system in orbit (e.g., interaction between the plume and the solar array orientation, leading to complex patterns for the spacecraft floating potential), which need appropriate modeling to be understood. Even before the application of electric thrusters in-flight, detailed on-ground characterization has to be performed. Also, in this case the need to decouple the interaction phenomena that occur between the thruster and its test facility is important to correctly design the thruster itself. Experience has shown that a complete 3-D simulation is desirable to understand these phenomena with a realistic description of the involved geometries, and that in many cases a completely particle approach (i.e., use of electron particles as well as neutral and ion particles) is needed, so that a detailed plasma-surface interaction model can be implemented.

II. The PICPluS Code Family

The PICPluS code family is composed of two- and three-dimensional hybrid/full particle in cell (PIC) codes, developed at Alta since 2002 ([1–8]). The codes allow one to perform time-accurate plasma plume/spacecraft interaction simulations in four different ways: 1) full particle simulation on a multiblock grid composed of Cartesian structured boxes with external solid surfaces, 2) full particle simulation on a nonstructured grid including surfaces and solid bodies (Fig. 1 and 2), 3) quasi-neutral simulation on a nonuniform structured grid including surfaces and solid bodies, and 4) quasi-neutral simulation on a general nonstructured grid including surfaces and solid bodies.

Hall effect thruster, gridded ion engines, and field emission electric propulsion thrusters can be simulated, and the application of the code to magnetoplasmadynamic thruster is presently underway. In the unstructured versions multiple thrusters firing simultaneously can be simulated and thrust steering device effects can be studied.

Typically, the plume is simulated starting from the thruster outlet using customizable inlet distributions. A general analytical model is used to statistically represent the desired distributions on the thruster exit for particle number density, position, and velocity vectors. The magnetic field can be added as a constant input field, allowing one to perform the full thruster simulation (i.e., including the ionization regions) provided that a relatively small grid is used to properly represent the Debye length. Usually, in this case a multidomain approach has to be used, simulating at first the ionization region and

---

Received 24 January 2008; revision received 21 September 2009; accepted for publication 30 September 2009.

[*] Project Manager; a.passaro@alta-space.com.

[†] Project Engineer; a.vicini@alta-space.com.

[‡] Project Engineer; f.nania@alta-space.com.

[§] Consultant; l.biagioni@alta-space.com.

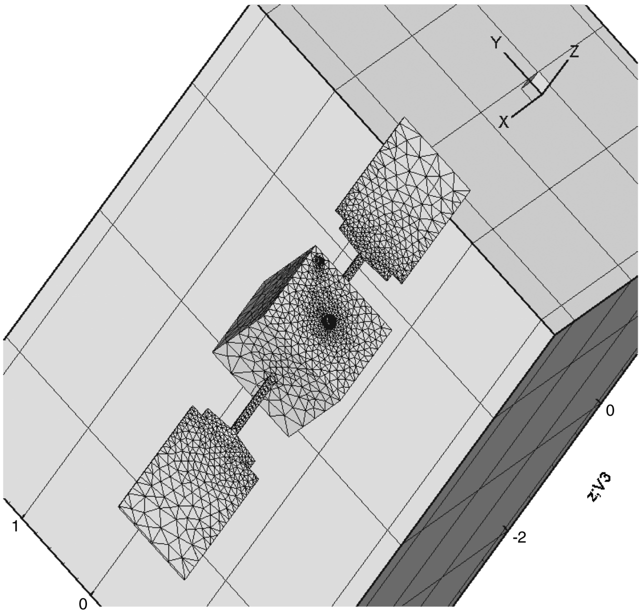

Fig. 1 PICPluS 3-D SMART-1 geometry model in the unstructured model.

using the output of the simulation for the plume simulation. Finally, the code is written with the aim of using as much experimental data as possible for the input, and is provided with internal advanced interpolation features (Fig. 3) to produce the proper input files, even starting from data on a small set of points. In the case of the completely unstructured code, an object-oriented approach has been implemented for the grid, particle, species, sources, and wall treatment, choosing as primary class the tetrahedral/triangular cells and considering the internal particles and the external boundaries as additional properties of the cell. The main advantage of this approach is the significant speed up that is obtained for the particle find at each iteration.

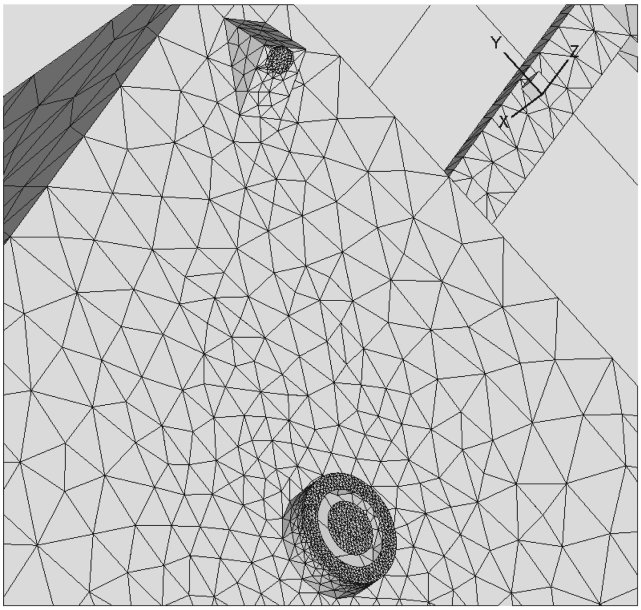

Fig. 2 Detail of the surface discretization of the thruster and the EPDP.

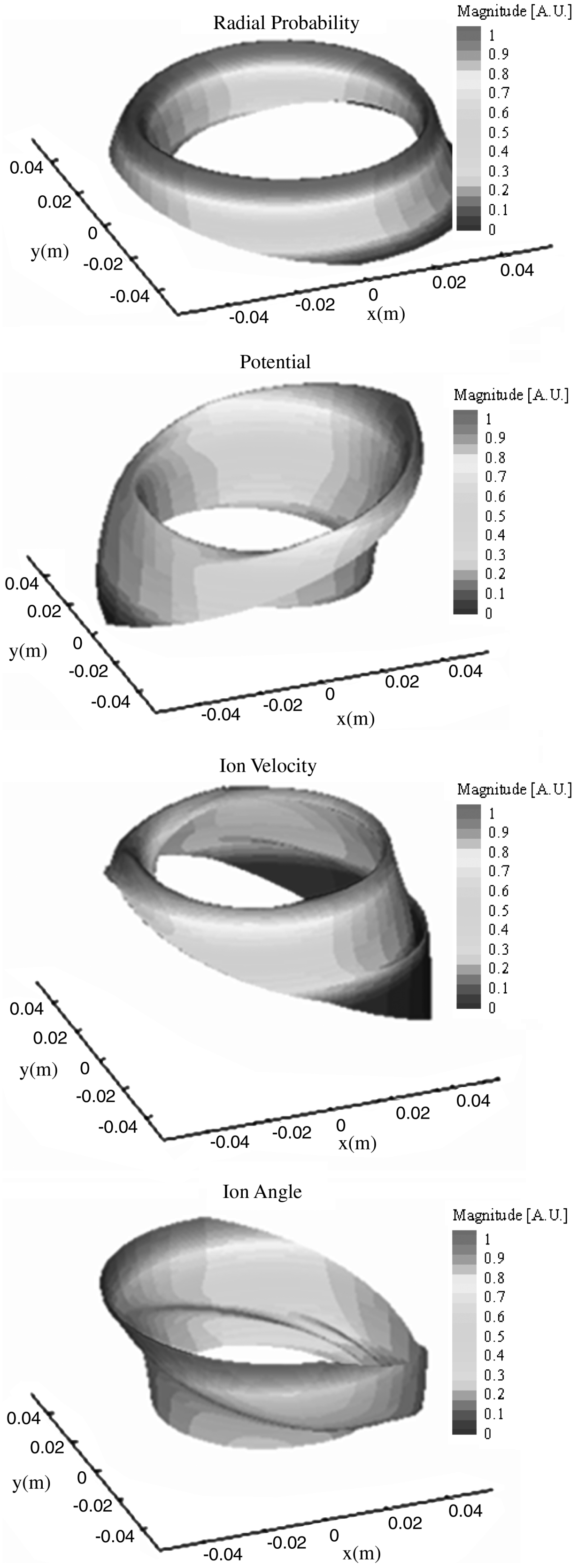

Fig. 3 3-D injection probability distributions obtained for non-axisymmetric inlet conditions.

The codes are written entirely in FORTRAN and are based on the MS Windows OS, with a user-friendly graphic user interface for the run setup. Because of the different approaches and the related memory requirements, different numbers of cells and particles can be simulated in sufficiently short times (typically one day of simulation on a standard single processor personal computer workstation), as indicated in Table 1. A parallel version is under development for application within UNIX/LINUX operative system on Sun Microsystems workstations.

Table 1 PICPluS 3-D typical limit parameters for runs on a single processor personal computer workstation

Model	Grid type	Maximum number of cells	Maximum number of particles
Structured hybrid	Nonuniform Cartesian with internal bodies	$2 \cdot 10^6$	$5 \cdot 10^6$
Unstructured hybrid	Tetrahedrons	$5 \cdot 10^5$	$2 \cdot 10^6$
Full particle	N Cartesian boxes	$N \cdot 17 \cdot 10^6$	$70 \cdot 10^6$
Full particle	Unstructured	$2 \cdot 10^5$	$1 \cdot 10^6$

A. Plasma Dynamics

1. Ions and Neutrals

Several particle species can be independently simulated (neutral atoms, single and doubly charged ions). Xenon and caesium are currently used as propellants, but other propellants can be added. Background distributions of neutral propellant can be included in the simulation to simulate the vacuum chamber environment. Neutral atoms, possibly exiting from the thruster due to the effective ionization rate, can be also simulated (either through a Monte Carlo collision [MCC] or direct simulation Monte Carlo [DSMC] approach). The injection energy distribution function is a Maxwellian distribution with random sampling considering three different temperatures for the three components of the velocity vector, and the evolution of the energy distribution is subsequently determined by the collisional processes leading to possibly different-than-Maxwellian distributions. If the ion is created by an ionization collision, it takes the velocity of the neutral originating it.

2. Electrons

If the full particle approach is used, electrons can be simulated as independent particles. Because of their low mass, an extremely small time step ($\sim 10^{-11}$ s) has to be used to have them move by less of the cell reference length in a single step, as experience has proven that inaccurate results are obtained if a step that is too big is used. In addition, the complete Poisson's equation has to be solved necessarily at each electron time step, leading to the need for fast 3-D solvers. Two additional techniques can be used to speed up the simulation: artificial decrease of the heavy particles mass, as indicated by [9], with the related decrease in the minimum required time step, and use of different time steps for each particle species while preserving the time-accurate approach. This approach was found to be inadequate for the ionization region simulations, leading to the need of full representative simulations and, therefore, long simulation durations. The technique of modification of the vacuum permeability ε_0 to increase the Debye length, also presented in [9], is not implemented in order not to sum nonlinear correction effects that could modify the simulated physics (in agreement with other authors, as shown in [10]). The electron injection energy distribution function is a Maxwellian distribution with random sampling considering the local electronic temperature value; the evolution of the energy distribution is subsequently determined by the collisional processes, leading to possibly different-than-Maxwellian distributions.

3. Potential and Electric Field

For the quasi-neutral codes, the electric potential is obtained from the superposition of the instantaneous potential field derived from the solid surfaces and the one created by the plasma. The plasma contribution to the total potential is obtained by the hypothesis of quasi neutrality, and thus equalling the electron density to the ion density. Assuming that electrons in the plume are collisionless and unmagnetized and that their pressure obeys the ideal gas law, the following equation system can be used:

$$\varphi - \varphi^* = \frac{kT_e}{e} \ln\left(\frac{n}{n^*}\right) + \tag{1}$$

$$T_e = \text{const} \tag{2}$$

or

$$\varphi - \varphi^* = \frac{k \cdot \gamma \cdot T_e^*}{e \cdot (\gamma - 1)} \left[\left(\frac{n}{n^*}\right)^{\gamma - 1} - 1 \right] + \tag{3}$$

$$T_e = T_e^* \left(\frac{n}{n^*}\right)^{\gamma - 1} \tag{4}$$

where the superscript $*$ indicates the reference state. The electron temperature in Eq. (1) is constant. However, as experimental evidence indicates that also in plume expansions the electron temperature is not constant, a polytropic model with exponent γ ([11]) can be used to relate its changes to changes in electron density at each time step [Eqs. (3) and (4)].

For the full particle code, instead, at each time step the complete Poisson equation is solved considering ion and electron density as well as the instantaneous values of potential on the surfaces. For the multiblock Cartesian grid code, the solver is a standard 3-D multigrid routine with uniform spacing on each direction (but not necessarily equal on the three axes), optimized for speed. For the unstructured codes the Poisson solver is based on the finite element discretization of the problem with the Galerkin weighted residual approach ([12]). Three different boundary conditions can be imposed for the potential calculation: constant potential, normal derivative equal to zero, and a mixed condition.

For all models the spacecraft (solid surface) floating potential calculation can be performed, at each time step or every n step, considering that its value is the one that implies a net current flux on that surface element equal to zero

$$I_{\text{ionic}} + I_{\text{electronic}} = 0 \tag{5}$$

Several components can be considered both for the ionic and electronic parts of Eq. (5) such as thermal, space ambient (including possible ram and wake effects), primary beam, and backflow components. Moreover, a more detailed simulation of each surface element can be imposed defining its properties in the preprocessing phase (e.g., constant potential, partial current flux entering, internal connection with other elements, etc.), thus allowing a fully coupled plume-charging analysis. In general, Eq. (6) is used to correlate the single component of current to the surface element floating potential

$$I = \pm \frac{e \cdot n \cdot A}{4} \sqrt{\frac{8 \cdot k \cdot T}{\pi \cdot m}} \cdot \exp^{\frac{e \cdot (V - V_f)}{k \cdot T}} \tag{6}$$

For the structured grid based simulations, the electric field is obtained through spatial differentiation of the plasma potential. For the unstructured grid case, the electric field is obtained on the grid nodes by computing the potential gradient. To this purpose a least-squares technique is used. The least-squares gradient reconstruction procedure originally developed by Barth ([13]) is based on approximating the variation of a dependent variable φ along an edge linking vertices 0 and i by a truncated Taylor series, for example, for a linear approximation

$$\phi_i = \phi_0 + (\nabla\phi)_0 \cdot \Delta\mathbf{r}_{0i}, \qquad 1 \le i \le d_0 \tag{7}$$

where $\Delta\mathbf{r}_{0i} = \mathbf{r}_i - \mathbf{r}_0$ and $\mathbf{r}$ are the position vectors. We define d_0 the degree of vertex 0, i.e., the number of neighbors included in the gradient reconstruction at vertex 0. The application of Eq. (7) to all edges incident to vertex 0 gives a system of linear equations for the derivatives at vertex 0, with a $d_0 \times n_0$ matrix of geometrical terms, (n_0 derivatives, d_0 function values). Because the degree is usually larger than the number of derivatives reconstructed, the system is solved in a least-squares fashion.

4. Virtual Probes and Diagnostics

Virtual retarding potential analyzer (RPA) and Faraday cup rakes can be placed anywhere in the flowfield, assigning to each probe its real dimension and normal vector. In the unstructured grid it is also possible to assign solid properties to the probes (surface mesh, surface temperature, and potential), although with a penalty on simulation speed due to the heavier grid requirements (Fig. 1). Additional virtual diagnostics include the computation of integral thruster performance parameter (thrust, discharge current) as well as distributions on all of the solid surfaces (impacts, currents, sputtering, etc.) and the calculation of population parameters such as, for example, the electron energy distribution function.

B. Particle Approach

1. Computational Grid and Multiblock Approach

For both the constructed grid based simulations, the grid is generated by simple input screens in the code GUI before the beginning of the simulation and successively stored in an output file for review. The PICPluS preprocessor therefore calculates a set of useful parameters as the grid spacing (nonuniform) and the boundary elements (internal and external surfaces).

For the unstructured-based simulation, the mesh can be generated using any available dedicated software and then fed to the preprocessor. The present code version uses as the default input grids produced by the code GMSH ([14]). After reading the list of nodes coordinates and connectivity, a number of quantities are computed and stored to make the grid usable by the PIC code. The most important among these can be summarized by the following actions: 1) identification and label of each single face as internal or boundary (outflow, wall, source, etc.), 2) find the list of all neighbor cells (i.e., all the cells that have at least one node in common with it) for each tetrahedron, and 3) find the list of all neighbor nodes (i.e., all the nodes connected with it through an edge) for each node.

All these operations are done only once for each mesh in the preprocessing phase, and the relevant data are stored in a grid file that is an input for the PIC code.

2. Particle Search

For the structured grid-based models, the particle search phase is almost automatic due to the simple analytical relations that relate any point in the domain with the correspondent cell. In the unstructured case, instead, no analytic relation relates the point in space occupied by a particle and the surrounding cell. A more complex algorithm is needed to individuate the cell containing the particle; obviously a simple loop on each cell is sufficient but extremely time consuming and, therefore, to be avoided if possible. To this regard an object orientation character is given to the code regarding the grid and particle treatment. The label of the cell containing each single simulated particle is computed and stored at each time step as a particle property. After injection, the cell containing the new particle is searched among those having one face on the thruster exit. The volume of the three tetrahedrons obtained by connecting the particle with the four nodes of a cell are computed; if the sum of these three volumes differs from the volume of the considered cell by less than a specified tolerance, the particle belongs to that cell. After the generic time step, each particle is first searched in the cell where it was at the beginning of that time step; if the particle is not found in that cell, the volume residual procedure previously described is carried out for each of the neighbor cells, and the particle is assigned to the cell where the residual has the minimum value.

When particles are found outside the domain a set of possible treatments is applied depending on the type of the boundary cell:

1) If the cell type is outflow the particle is deleted.

2) If the cell type is solid surface the particle can be deleted or scattered with an input-derived accommodation coefficient.

3) If the simulation takes into account surface charge for floating potential calculation or Hall Effect Thruster channel simulation, a bouncing ion can be neutralized and reemitted as a neutral, and a bouncing electron can generate secondary emission.

4) Secondary electron emission is based on the model described in [10].

3. Collision Dynamics

Neutral–neutral, neutral–electron, and ion–neutral (elastic and charge exchange) collisions can be included in the PIC cycle independently, whereas electron–electron and electron–ion collisions are usually treated via an analytical MCC model. Typically the variable hard sphere model is employed ([15,16]), and, for Xenon atom–ion collisions, also the induced dipole model of Nanbu ([17,18]) can be used. In the latter case, no collision cross sections need to be modeled.

More in detail, in the induced dipole interaction model ([17]), the collision probability of ion A with molecule B in time Δt takes the form

$$P_c = n_B (8a/\mu)^{1/2} \pi \beta_\infty^2 \Delta t \tag{8}$$

where $a = \alpha_d e^2/[2(4\pi\varepsilon_o)^2]$, $\alpha_d/(4\pi\varepsilon_o)$ is the polarizability of the molecule, $\mu = m_A m_B/(m_A + m_B)$ is the reduced mass, and β_∞ is the cutoff value of the dimensionless impact parameter $\beta = b(\varepsilon/4a)^{1/4}$.

Here $\varepsilon = \mu g^2/2$ is the relative collision energy, $g = |\boldsymbol{v}_A - \boldsymbol{v}_B|$ is the relative speed, and b is the impact parameter. Note that P_c expressed by Eq. (1) is constant in each cell, meaning that any molecule B is equally probable as a collision partner of ion A; a partner molecule can be randomly sampled from the set of molecules in a cell.

In Nanbu's variable hard sphere ([18]), the probability that molecule A_i collides with some molecule B_j in Δt is

$$P_{Ai} = n_B \langle g \sigma_T^{AB} \rangle \Delta t \tag{9}$$

where σ_T^{AB} is the total cross section for $A - B$ collisions. The average is for all simulated molecules B in a cell, and Eq. (10) takes the form $P_{Ai} = \sum_{N_B} P_{Ai,Bj}$, where $P_{Ai,Bj} = N_B^{-1} n_B g_{Ai,Bj} \sigma_T^{AB}$ and Δt is the probability that molecule A_i collides with molecule B_j in Δt (n_B is the number density, WN_B/V_c). The cross section σ_T^{AB} is a function of $g_{Ai,Bj} = |\boldsymbol{v}_{Ai} - \boldsymbol{v}_{Bj}|$. An estimate of the maximum relative speed $g_{\max}^{AB}$, is given by

$$2.5\sqrt{2kT_{\text{ref}}/\mu_{AB}}$$

Finally, in the more classical Szabo variable hard sphere method ([9]), given an ion of velocity $\boldsymbol{v}$ and a neutral background with number density n_B, the ion collision frequency is computed as

$$\nu = g \sigma_T(g) n_B \tag{10}$$

where $\sigma_T(g)$ is the total cross section. Each time an ion is moved, the collision probability in the time step Δt is $p = 1 - e^{-\nu \Delta t}$. We compare this to a random number U. If $U < p$ a collision occurs. The probability of a charge exchange is given by the ratio of the charge exchange (CEX) collision cross section and the total collision cross section.

For elastic (scattering) collisions, the following cross section is used for both $\mathrm{Xe} - \mathrm{Xe}^+$ and $\mathrm{Xe} - \mathrm{Xe}^{++}$ collisions ([19]):

$$\sigma_{\text{EL}}(g) = 6.42 \times 10^{-16}/g\ \text{m}^2 \tag{11}$$

For charge exchange collisions the following cross section is used ([20]):

$$\sigma_{\text{CEX}}(g) = [k_1\, \ell n(g) + k_2] \times 10^{-20}\ \text{m}^2 \tag{12}$$

where $k_1 = -0.8821$ and $k_2 = 15.126$ for single charged ions, and $k_1 = -2.704$ and $k_2 = 36$ for doubly charged ions.

The ionization cross section, and ion–ion, ion–electron, and electron–electron cross sections are directly taken from [9].

No anomalous diffusion is considered for Hall effect thruster channel simulations.

4. Boundary Conditions

The boundaries of the simulation domain can be considered as outflow or as solid walls. In the latter case their initial temperature and potential are assigned and can be kept constant during the simulation; if the unsteady simulation is chosen the values are updated at each time step. Particle impacts may range between perfect reflection and full random diffusion, with partial thermal accommodation calculated using Cercignani–Lampis–Lord model

Table 2 Validation test case matrix [8]

Thruster model	Vd, V	Id, A	Anode mass flow rate, mg/s	Background pressure, mbar
SPT-100	300	4.5	4.99	$2.9 \cdot 10^{-6}$
SPT-100	300	4.5	5.12	$4 \cdot 10^{-5}$
SPT-100	300	4.5	5.084	$5.32 \cdot 10^{-5}$
PPS-1350	350	3.47	4.21	$1 \cdot 10^{-4}$
Alta XH5	350	11.16	9.2	$8.32 \cdot 10^{-5}$
MUSES-C	1500	0.14	0.21	$2.0 \cdot 10^{-6}$

([16]). In the same manner internal solid boundaries can be modeled. Regarding the Poisson equation solution, boundary conditions are the classical Dirichlet, Neumann, and mixed conditions.

Atoms, ions, and electrons are injected from the plasma-injecting boundaries probabilistically sampling their properties from distributions for number density, temperature, and velocity based on the injection position (e.g., the radius in a Hall effect thruster). The distributions are derived from experimental data found in literature or in-house experiments with an internal interpolation routine or analytically imposed as polynomials and exponentials.

III. Code Verification and Validation

The single code models have been verified and validated in the last few years through comparison with data available from literature and from internal tests at Alta. Application of the code to flight data was carried out within the SMART-1 Plasma Working Group lead by ESA. Table 2 summarizes the main test cases used for validation. Generally speaking, good agreement was achieved with respect to thrust, ion beam current, and ion current densities up to 90 deg from thruster exit.

A. SPT-100

Data measured by Kim et al. [21], King [22], Manzella and Sankovic [23], and Manzella [24] were satisfactorily reproduced using a single set of injection conditions by PICPluS 3-D code as shown in Fig. 4. From a physical point of view it appears that, for an axisymmetric simulation, slightly higher levels of electron temperature are obtained in the near field with respect to the 3-D results, starting from exactly the same initial conditions.

B. PPS®1350

Data measured during a ground test of the PPS®1350 were made available by Snecma for a Faraday cup rake situated 0.65 m from the thruster exit and run with a probe bias of some volts. Of course, as already mentioned by Van Gilder and Boyd in [25], the most important parameter determining plume behavior appears to be the inlet distributions used for ion injection. Starting from the SPT-100 typical inlet distributions it was possible to identify the injection parameters able to best reproduce the experimental data, obviously including a proper probe bias, that were then used for 2-D and 3-D simulations. The two codes' results agree fairly well (Fig. 5) with respect to simulations of ground conditions, whereas a certain discrepancy (about 5 deg) can be distinguished in simulations of flight conditions at angles greater than 30 deg, due to the heavy effect that, in this case, is played by the electron temperature model.

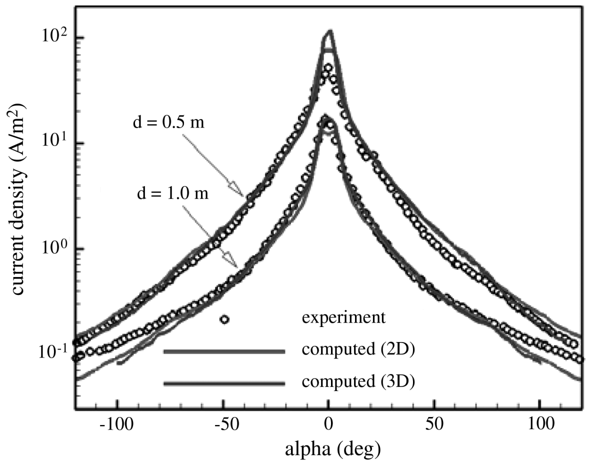

Fig. 4 Comparison between 2-D, 3-D, and experimental data by King [22] for the SPT-100 thruster in vacuum chamber conditions.

IV. Application to the SMART-1 Flight Data

SMART-1 is the first ESA conceived to demonstrate the operation and the effectiveness of the solar electric propulsion for deep space cruising in preparation of future ESA Cornerstone missions. Successfully launched on 27 September 2003, the SMART-1 satellite reached the moon orbit on 27 February 2005 and its orbit period was extended due to a smaller than expected propellant usage up to that point. The selected strategy for the orbit raising consisted of extensive Hall effect thruster (HET) use for progressive expansion of the spacecraft orbit, spiraling out from the initial geosynchronous transfer orbit (GTO) until the spacecraft was caught by the moon's gravitational field. The monitoring of the operation/environment of the electric propulsion (EP) system, during the orbit transfer from GTO to the final lunar orbit, was retained as a key element of the SMART-1 technology objectives. For this task a specific instrument, the electric propulsion diagnostic package (EPDP) shown in Fig. 6, was developed by Thales Alenia Space Italia ([26]). The EPDP operates on SMART-1 in conjunction with another instrument,

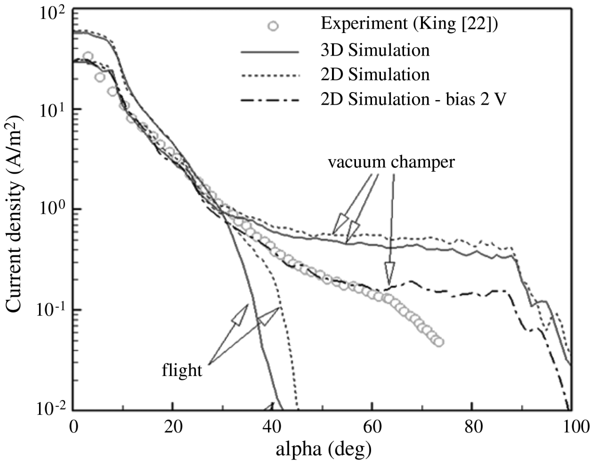

Fig. 5 Comparison between 2-D, 3-D, and experimental data for the PPS-1350 thruster in vacuum chamber conditions.

Fig. 6 The Thales Alenia Space EPDP unit.

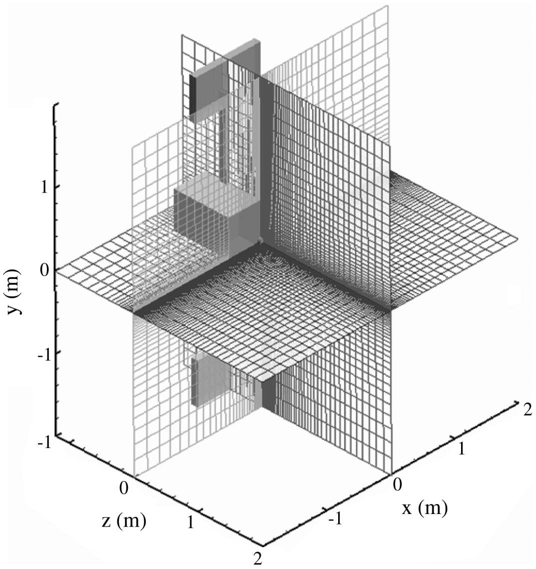

Fig. 7 General nonuniform structured grid for the SMART-1 simulations.

SPEDE (Spacecraft Potential Electron and Dust Experiment), to achieve a comprehensive evaluation of performance and effects of the HET EP based on the PPS®1350 thruster developed by SNECMA. Whereas the EPDP provides information on the plasma environment near the thruster, SPEDE characterizes the plasma on the spacecraft sides. The EPDP on SMART-1 is primarily intended to be operated, together with the thruster, during the spiraling escape maneuvers around the Earth and the capture into the moon's orbit. The EPDP can be operated according to a suitable set of commands and collects information on the following: 1) energy/current distribution of plasma ions close to the plasma beam, 2) plasma electronic parameters (e.g., plasma density, potential and electron temperature), 3) material erosion/deposition at the quartz crystal microbalance location, and 4) solar cell performance (V-I measurement in open, load, short condition).

A. Simulation Results: Comparison with Flight Data and Analysis for the Retarding Potential Analyzer

A set of numerical simulations was executed with the PICPluS 3D on the grid shown in Fig. 7 considering for all of the cases the standard injection conditions shown in Table 3. The results were compared with EPDP data considering a virtual RPA probe placed in the exact EPDP location, and considering plasma features at the same place.

Looking at the RPA flight data (Fig. 8) two peculiar features are evident: first, the energy distribution presents a plateau after the primary peak with a long tail reaching energies up to 100 eV, compatible with the presence of a secondary peak situated about 20 V after the first. Secondarily, the primary peak seems to have a somewhat higher-than-expected energy, and a peculiar absence of low-energy impinging ions is noted.

Table 3 Simulation parameters

Mass flow rate	$4.21 \cdot 10^{-6}$ kg/s
Discharge voltage	350 V
Discharge current	3.47 A
Thrust	72.1 mN
Background pressure	$1 \cdot 10^{-9}$ Pa
Ionization efficiency	90%
Percentage of Xe^{++}	0–25%
Electron temperature model	Adiabatic or constant
Potential field	Quasi neutral
Potential on solid walls	0 V
Neutral atoms plume	Precomputed

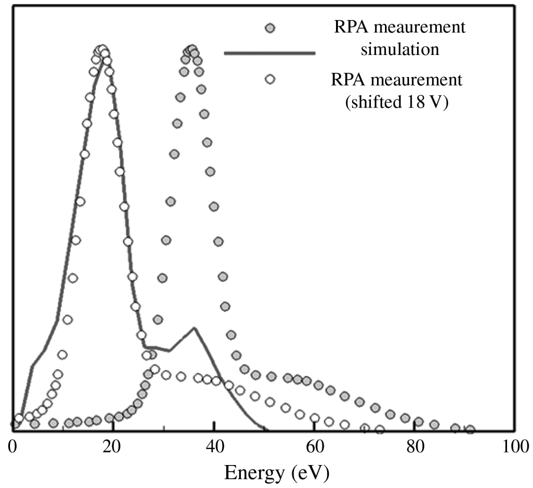

Fig. 8 Comparison between numerical results and flight data for the RPA measurements.

The first set of simulations, conducted with the polytropic model for electron temperature (with typical value of about 8 eV at the channel exit and $\gamma = 4/3$) produced a remarkably similar pattern for the RPA measurement, although shifted by almost exactly 18 V toward lower energies. At the same time, it was noted from flight data that an almost constant gap of 18 V was present between RPA first peak position and the satellite floating potential. The explanation to this feature becomes evident considering that the RPA ground is given from the floating potential; incoming ions with energy in the plasma plume of about 18 eV are accelerated by an amount exactly equal to the floating potential by the RPA grid (summed with its sheath potential drop, that should be of some volts) before being collected.

In any case, it was decided to extend the investigation in two different directions: assessment of the effect of the electron temperature model and actual value on the results, and assessment of the effect of the presence of Xe^{++} ions in the flow leaving the thruster. A total of eight numerical test cases were run with the results summarized in Table 4 for the six runs concerned with the electron temperature model.

For what concerns the electron temperature model effect it appears that, using the polytropic model, realistic values for T_e and ion number density are obtained in the EPDP position compared with the flight data. It can be noted that the instrument seems to lay on the edge of the plasma plume and, therefore, is subjected to relatively high variations of ion number density (e.g., for case 1 between $3.7 \cdot 10^{13}$ and $7 \cdot 10^{13}$ m^{-3}); the possibility of the EPDP location within the plasma sheath is consistent with the fact that the EPDP identified a slightly nonneutral plasma. As expected from Eq. (3), in the case of nonconstant T_e, the plasma potential of the satellite surfaces is always predicted as slightly negative (1.5–4.5 V) with respect to the plasma potential, assuming $\varphi = 0$ V at infinite distance from the satellite. An increase in the T_e reference value corresponds to a shift of the RPA peaks toward higher values with an overall broadening of the primary peak and an increasing separation of the two peaks; a significant part of low-energy events is recorded in any case (Fig. 9).

The use of a constant value for T_e produces RPA distributions that are closer to the flight data for what concerns the low-energy values, but usually tend to present a secondary peak that is too high with respect to the first one (Fig. 10). Electron temperature value and relative potential are extremely different from the recorded ones, and ion number density is less than expected and close to the low limits for the adiabatic cases. An increase in the temperature value produces a significant shift of the peaks toward higher energies (as also noted by Boyd in [27]).

Considering the effects of the chosen electron temperature model on the whole plume shape (Fig. 11), one can observe that, in general, an increase of the reference T_e produces a wider plume with a stronger expansion in the axial direction. The choice of constant

Table 4 Simulation results compared with electric propulsion diagnostic package data

Case	T_e model	T_e reference, eV	Collisions model	Retarding Potential Analyzer Peak 1, V	Retarding Potential Analyzer Peak 2, V	Peak distance, V	Full width at half maximum, V	Electric propulsion diagnostic package relative potential, V	Electric propulsion diagnostic package Te, eV	Electric propulsion diagnostic package $n_i \times 10^{13}$, m^{-3}
1	Polytropic	8	Nanbu	18.8	36.1	17.3	12.9	+1.99	0.50	3.7–7
1b	Polytropic	8	VHS	19.0	38.5	19.5	12.8	+2.23	0.56	3.6–7.2
2	Polytropic	12	Nanbu	27.1	49.2	22.1	13.5	+3.99	1.00	7–9
3	Polytropic	16	Nanbu	33.5	68.4	34.9	19.1	+4.4	1.10	5.4–6.8
4	Constant	3	Nanbu	26.3	43.8	17.5	11.6	+24.0	3.00	4.1
5	Constant	8	Nanbu	68.0	128.0	60.0	39.0	+64.0	8.00	3.2
6	Polytropic unstructured	8	VHS	17.92	38.5	20.58	13.4	+1.4	0.35	1.2–5
Electric propulsion diagnostic package flight data				35.6	55	19.4	13	+4	0.62–0.72	6.8–8.7

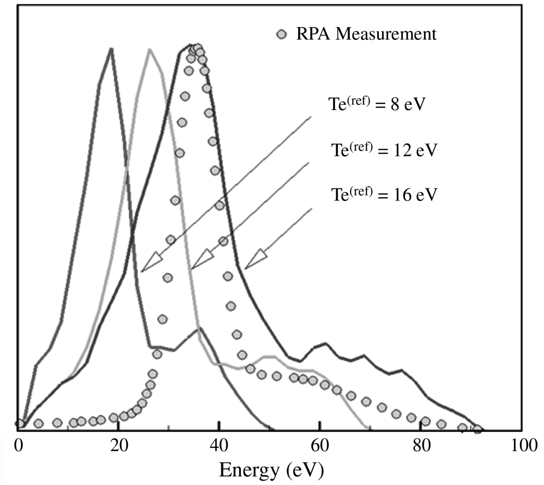

Fig. 9 Effect of polytropic model for electron temperature.

electron temperature tends to spread the CEX cloud that forms close to the satellite wall due to the migration of the CEX ions that are mainly generated at the exit of the acceleration channel. Nonetheless, plume shape and number density level are not extremely different in all of the considered test cases, except for the unstructured case that shows a more diffuse distribution in the backflow and predicts slightly lower values of ions, electrons, and electron temperature. Summarizing these considerations, it seems that the best way to reproduce the measured data is using the polytropic T_e model with a reference electron temperature between 8 and 12 eV, considering the shift to be imposed on the experimental data due to the grounding at the floating potential and a slightly different choice for γ.

To correctly reproduce the on-ground measured current density profiles and thruster parameters (thrust, discharge current), a significant amount of doubly charged Xenon ions has to be considered. The presence of Xe^{++} ions at the exit of a HET channel has been experimentally observed in several cases (for instance, see [21,23]), with their fraction increasing with the discharge voltage. The effect of the doubly charged ions presence is evidenced in Fig. 12 where it can be noted that, if no Xe^{++} are simulated, the RPA profile is completely different from the flight one, and a percentage of at least 20% of Xe^{++} seems needed to reproduce the second peak and plateau features. This is in accord with basic theoretical calculations on thruster performance, that see as necessary a similar percentage of doubly charged ions to have the prescribed discharge current, voltage, and thrust. On the other hand, the possibility of charge exchange collision involving doubly charged ions creating fast single charged ones could imply a different percentage of starting Xe^{++} ions.

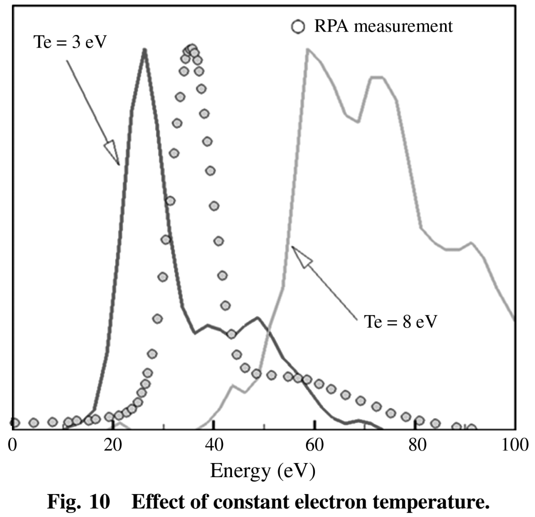

Fig. 10 Effect of constant electron temperature.

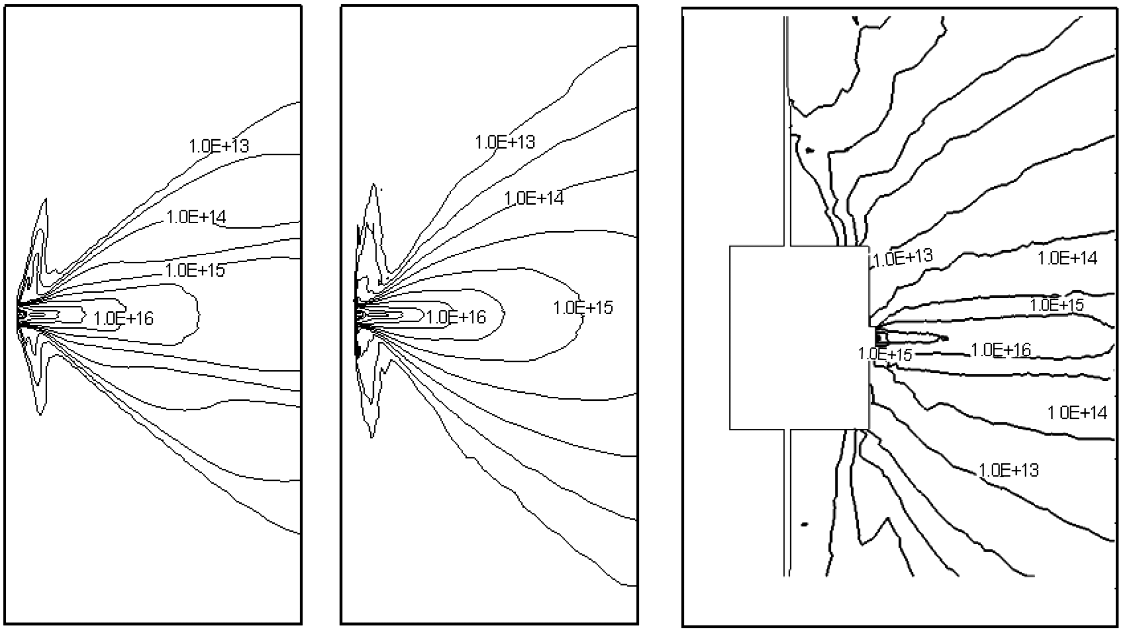

Fig. 11 Comparison between computed ion number densities for test cases 1, 5, and 6.

Finally, it has to be noted that as it was likely to be expected, the simulations for flight conditions predict a higher thrust level (up to +10%) than the one measured on-ground and this feature has been observed consistently within the more than 2000 hours of firing of the thruster for the orbit raising.

B. Interaction with the Solar Array and Advanced Simulations

For the whole mission duration, the flight instruments showed a variation of the floating potential during each orbit with values ranging between −5 V and +10 V approximately with respect to the cathode reference potential. The feature appeared to be consistently related to the solar array (SA) orientation with respect to the sun, therefore indicating a possible interaction between the SA and the thruster plume. The SA presents a front side, covered by protective glass, with underlying cell sections biased to 0– + 50 V and a back side with interconnectors that are not shielded from the surrounding plasma. The situation was modeled with PICPluS with SA rotation angle varying by 30 deg increments (Fig. 13). The calculation of the floating potential was therefore carried out using Eqs. (5) and (6) considering at first perfect and zero insulation on the front side (i.e., electric field generated by the SA potential completely shielded by the plasma or the opposite). Later on, to go into more detail, different levels of potential shielding for the glass-covered front part were considered (0, 25, 50, and 100%). Because the fine mesh needed to properly model the interconnectors was unfeasible in terms of memory requirements, the interconnector side was treated in a statistical (i.e., they were not modeled on the actual geometry, but a given probability corresponding to the interconnector/solar panel area ratio was given to each particle impacting the back surface of the panel to actually modify the spacecraft potential).

The results showed that from the thruster point of view, no appreciable difference in the plume is present. In particular, the RPA measurement wasn't changed by the rotation of the SA (Fig. 14). On the other hand, the plasma potential with respect to the imposed satellite potential varies with a trend similar to the measured one. The simulation with the more accurate description of the panel behavior led to variations in the floating potential consistent with the recorded pattern, although significantly lower in values (Fig. 15).

A final simulation was performed including the detailed EPDP geometry (Fig. 2): the results are in agreement with the previous

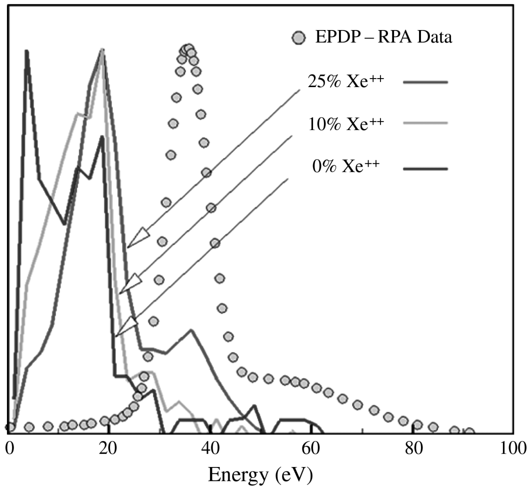

Fig. 12 Comparison between numerical results and flight data for the RPA measurements concerning the Xe^{++} population.

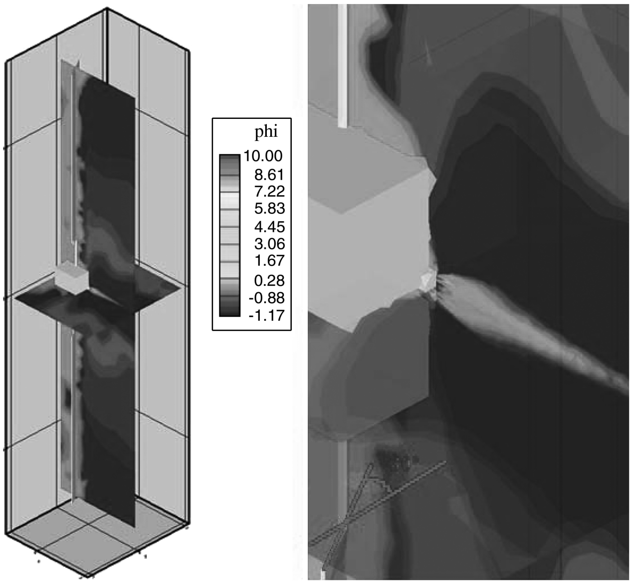

Fig. 13 Floating potential advanced simulation: full satellite modeled with 30 deg oriented solar panels.

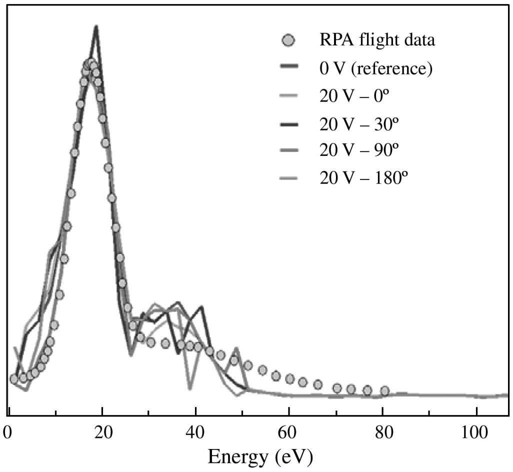

Fig. 14 RPA values in function of SA rotation: no significant difference is found.

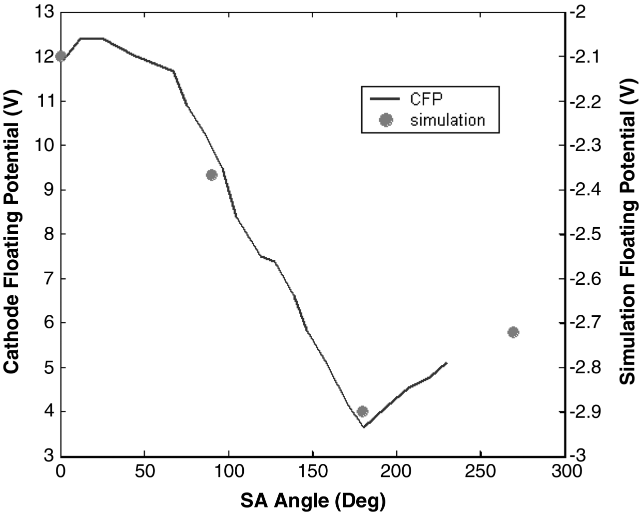

Fig. 15 In-flight cathode floating potential compared with simulation results for floating potential varying the SA orientation (50% shielding).

ones, although a different shape of the flow around the instrument can be seen (Fig. 16): the effect of the device body, as expected, increases the sheath dimension in its location further implying that the sensing element was placed on the sheath edge considering the spacecraft scale.

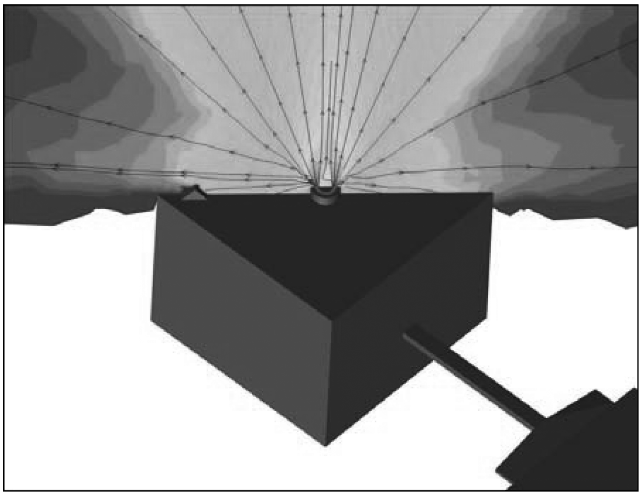

Fig. 16 Detail of the flow on the EPDP axis plane.

V. Conclusions

During the last few years Alta dedicated consistent efforts to individuate and develop a series of simulation instruments that can be used for design or diagnostic purposes. This paper focused on the PICPluS code family, illustrating at first the different physical and numerical models that are implemented in the codes. The results of the validation activity versus literature and experimental data were therefore presented. Finally, the results obtained for the SMART-1 satellite and their comparison with the in-flight data provided by the satellite instruments were presented. The RPA data were reconstructed satisfactorily and an analysis of the influence of electron temperature model and of the presence of doubly charged ions was subsequently conducted. The interaction of the thruster plume with the SA was also investigated showing that the effects on the thruster itself are limited, while imposing a greater influence on the satellite, especially with respect to its floating potential. Advanced simulations carried out with the 3-D unstructured code allowed correct reconstruction of the floating potential variation with SA orientation and better specification of the flow around the EPDP.

Acknowledgments

The authors wish to acknowledge the help provided by Jose Gonzalez del Amo and Eric Gengembre of European Space Agency-European Space Research and Technology Centre as lead persons of the SMART-1 Plasma Working Group, Thales Alenia Space Italia for the electric propulsion diagnostic package in-flight data, and Snecma Moteurs for the PPS®1350 ground-test data.

References

[1] Andrenucci, M., Biagioni, L., and Passaro, A., “PIC/DSMC Models for Hall Effect Thruster Plumes: Present Status and Ways Forward,” AIAA, Reston, VA, Paper 2002–4254, July 2002.

[2] Biagioni, L., Passaro, A., and Vicini, A., “Plasma Thruster Plume Simulation: Effect of the Plasma Quasi Neutrality Hypothesis,” *34th AIAA Plasmadynamics and Lasers Conference*, AIAA, Reston, VA, Paper 2003–4173, 2003.

[3] Passaro, A., Vicini, A., Nania, F., and Biagioni, L., “Numerical Rebuilding of SMART-1 Plasma Plume-Spacecraft Interaction,” International Electric Propulsion Conference, Princeton, NJ, Paper IEPC-2005-174, 2005.

[4] Passaro, A., Vicini, A., and Biagioni, L., “Plasma Thruster Plume Simulation: Effect of Vacuum Chamber Environment,” *35th AIAA Plasmadynamics and Lasers Conference*, AIAA, Reston, VA, Paper 2004–2357, 2004.

[5] Passaro, A., Vicini, A., and Biagioni, L., “3-D Computation of Plasma Thruster Plumes,” *40th AIAA/ASME/SAE/ASEE Joint Propulsion Conference & Exhibit*, AIAA, Reston, VA, July 2004.

[6] Passaro, A., Vicini, A., Nania, F., and Biagioni, L., “Numerical Rebuilding of SMART-1 Plasma Plume-Spacecraft Interaction,” *29th International Electric Propulsion Conference*, International Electric Propulsion Conference, Princeton, NJ, Paper 2005-174, 2005.

[7] Passaro, A., Nania, F., and Vicini, A., “Full 3D PIC simulation of Hall Effect Thrusters,” *37th AIAA Plasmadynamics and Lasers Conference*, AIAA, Reston, VA, Paper 2006–3246, 2006.

[8] Passaro, A., Vicini, A., and Nania, F., “Validation Status of the PICPluS Plume Simulation and Spacecraft Interaction Tools: Lesson Learnt from Flight and Ground Experimental Data,” *30th International Electric Propulsion Conference*, International Electric Propulsion Conference, Princeton, NJ, Paper 2007-325, 2007.

[9] Szabo, J. J., “Fully Kinetic Numerical Modeling of a Plasma Thruster,” Ph.D. Dissertation, Aeronautics and Astronautics Dept., Boston Univ., Cambridge, MA, 2001.

[10] Taccogna, F., Longo, S., Capitelli, M., and Schneider, R., “Seven Years of Hall Thruster Modeling: A European Collaboration Between Bari and Greifswald,” *30th International Electric Propulsion Conference*, International Electric Propulsion Conference, Princeton, NJ, Paper 2007-012, 2007.

[11] Celik, M., Santi, M., Cheng, S., Martinez-Sanchez, M., and Peraire, J., “Hybrid-PIC Simulation of a Hall Thruster Plume on an Unstructured Grid with DSMC Collisions,” International Electric Propulsion Conference, Princeton, NJ, March 2003.

[12] Zienkiewicz, C., “The Finite Element Method in Engineering Science,” McGraw–Hill, London, 1977.

[13] Barth, T. J., “A 3D Upwind Euler Solver for Unstructured Meshes,” AIAA, Reston, VA, Paper 91–1548, 1991.

[14] Geuzaine, C., and Remacle, J. F., “Gmsh: A Three-Dimensional Finite Element Mesh Generator With Built-in Pre- and Post-Processing Facilities,” http://geuz.org/gmsh/.

[15] Bird, G. A., *Molecular Gas Dynamics and the Direct Simulation of Gas Flows*, Oxford Science Publications, Oxford, 1994.

[16] Birdsall, C. K., and Langdon, A. B., *Plasma Physics via Computer Simulation*, McGraw–Hill, New York, 1985.

[17] Nanbu, K., and Kitatani, Y., “An Ion-Neutral Species Collision Model for Particle Simulation of Glow Discharge,” *Journal of Physics D: Applied Physics*, Vol. 28, No. , 1995, pp. 324–330.

[18] Nanbu, K., “Probability Theory of Electron-Molecule, Ion-Molecule, Molecule-Molecule, and Coulomb Collisions for Particle Modeling of Materials Processing Plasmas and Gases,” *IEEE Transactions on Plasma Science*, Vol. 28, No. 3, 2000, pp. 971–990.

[19] Dalgarno, A., McDowell, M. R. C., and Williams, A., “The Mobility of Ions in Unlike Gases,” *Proceedings of the Royal Society of London*, Vol. 250, Apr. 1958, pp. 411–425.

[20] Rapp, D., and Francis, W. E., “Charge Exchange Between Gaseous Ions and Atoms,” *Journal of Chemical Physics*, Vol. 37, No. 11, 1962, pp. 2631–2645.

[21] Kim, S. W., Foster, J. E., and Gallimore, A. D., “Very Near Field Plume Study of a 1.35 kW SPT-100,” AIAA, Reston, VA, Paper 96–2972, 1996.

[22] King, L. B., “Transport Property and Mass Spectral Measurements in the Plasma Exhaust Plume of a Hall Effect Space Propulsion System,” Ph.D. Dissertation, Dept. of Aerospace Engineering, Univ. of Michigan, Ann Arbor, MI, May 1998.

[23] Manzella, D. H., and Sankovic, J. M., “Hall Thruster Ion Beam Characterization,” AIAA, Washington, D. C., Paper 95–2927, 1995.

[24] Manzella, D. H., “Stationary Plasma Thruster Plume Emissions,” *23rd International Electric Propulsion Conference*, International Electric Propulsion Conference, Princeton, NJ, Paper 93-097, 1993.

[25] Van Gilder, D. B., and Boyd, I. D., “Particle Simulations of the SPT-100 Plume,” AIAA, Reston, VA, Paper 98-3797, 1998.

[26] Matticari, G., Noci, G., Estublier, D., Gonzales del Amo, J., Marini, A., and Tajmar, M., “The Smart-1 Electric Propulsion Diagnostic Package,” *Proceedings of the 3rd Spacecraft Propulsion Conference*, edited by R. A. Harris, European Space Agency, Cannes, France, 2000.

[27] Boyd, I. D., “Hall Thruster Far Field Plume Modeling and Comparison with EXPRESS Flight Data,” AIAA, Reston, VA, Paper 2002-0487, 2002.

J. Blandino
Associate Editor